Earth Planets Space, **64**, 1005–1021, 2012

Approximate treatment of seafloor topographic effects in three-dimensional marine magnetotelluric inversion

Noriko Tada[1,2], Kiyoshi Baba[2], Weerachai Siripunvaraporn[2,3,4], Makoto Uyeshima[2], and Hisashi Utada[2]

[1]*Institute for Research on Earth Evolution, Japan Agency for Marine-Earth Science and Technology, 2-15 Natsushima, Yokosuka, Kanagawa 237-0061, Japan*
[2]*Earthquake Research Institute, University of Tokyo, 1-1-1 Yayoi, Bunkyo-ku, Tokyo 113-0032, Japan*
[3]*Department of Physics, Faculty of Science, Mahidol University, Rama VI Road, Rachatawee, Bangkok 10400, Thailand*
[4]*ThEP Center, Commission on Higher Education, 328, Si Ayutthaya Road, Bangkok 10400, Thailand*

(Received July 14, 2011; Revised April 6, 2012; Accepted April 7, 2012; Online published November 26, 2012)

Seafloor magnetotelluric (MT) observations using ocean bottom electromagnetometers (OBEMs) provide information on the electrical conductivity structure of the oceanic mantle. A three-dimensional (3-D) analysis is particularly important for marine MT data because the electric and magnetic fields observed on the seafloor are distorted by the rugged seafloor topography and the distribution of land and ocean. Incorporating topography into 3-D models is crucial to making accurate estimates of the oceanic mantle's conductivity structure. Here we propose an approximate treatment of seafloor topography to accurately incorporate the effect of topography without significantly increasing the computational burden. First, the topography (lateral variation in water depth) is converted to lateral variation in effective conductivity by volumetric averaging. Second, we compute the electric and magnetic field components used to calculate the MT responses at arbitrary points from the electric field components on staggered grids, using a modified interpolation and extrapolation scheme. To verify the performance of this approximate treatment of seafloor topography in 3-D inversions, we tested the method using synthetic seafloor datasets and both 3-D forward modeling and inversion. The results of the synthetic inversions show that a given conductivity anomaly in the oceanic upper mantle can be recovered with sufficient accuracy after several iterations.

Key words: Marine magnetotellurics, topographic effects, 3-D inversion, electrical conductivity.

1. Introduction

Magnetotelluric (MT) sounding is a powerful geophysical method to explore the Earth's interior structure using its electrical conductivity. The electrical conductivity of Earth materials is known to be strongly dependent on physical conditions such as temperature, water content, and degree of partial melting (e.g., Yoshino, 2010; Yoshino *et al*., 2010) which control their mechanical properties. Especially in oceanic areas, therefore, a number of efforts have been made to obtain accurate images of the electrical conductivity distribution in the upper mantle since Filloux's (1973) pioneering work was published.

In earlier times, one-dimensional (1-D) interpretation was the only way to infer the electrical conductivity distribution below the ocean bottom due to limits on either the number of observation sites or inversion techniques in higher dimensions (e.g., Filloux, 1981; Oldenburg, 1981). The number of instruments employed in each experiment has increased in recent years allowing researchers to attempt two-dimensional (2-D) inversions (e.g., Evans *et al*., 1999; Matsuno *et al*., 2010) or 1-D inversions assuming the presence of 3-D heterogeneity (e.g., Baba *et al*., 2010).

doi:10.5047/eps.2012.04.005

However, several technological difficulties that hamper inversion of seafloor MT data must be overcome to obtain accurate 3-D electrical conductivity images at a regional mantle scale. This paper deals with one such difficulty, the so-called topographic effect (e.g., Nolasco *et al*., 1998; Baba and Seama, 2002). The electric and magnetic (EM) fields observed on the seafloor are generally distorted in any direction by rugged seafloor topography, which is more significant than the effect such topography has on land MT data (e.g., Nam *et al*., 2008) because of seawater's extremely high conductivity, which produces strong contrast at the seafloor (Schwalenberg and Edwards, 2004). In recent years, several works have attempted to solve the problem of topographic effects on seafloor MT data. Baba and Chave (2005) proposed a scheme to correct 3-D topographic effects, which was applied to 2-D inversion of seafloor MT results on a regional scale (Baba *et al*., 2006). Li *et al*. (2008) pointed out that such an approach might be effective for exploring large-scale structures but not for studying fine-scale subsea structures, and suggested another approach in which topography is explicitly incorporated into 2-D inversion using finite-difference approximations.

For an accurate estimation of deep mantle conductivity distributions in 3-D, these topographic effects have to be properly and accurately taken into account in the inversion. In reality, topography variations occur over a wide range of horizontal scales from local (∼100 m) to regional (∼1000

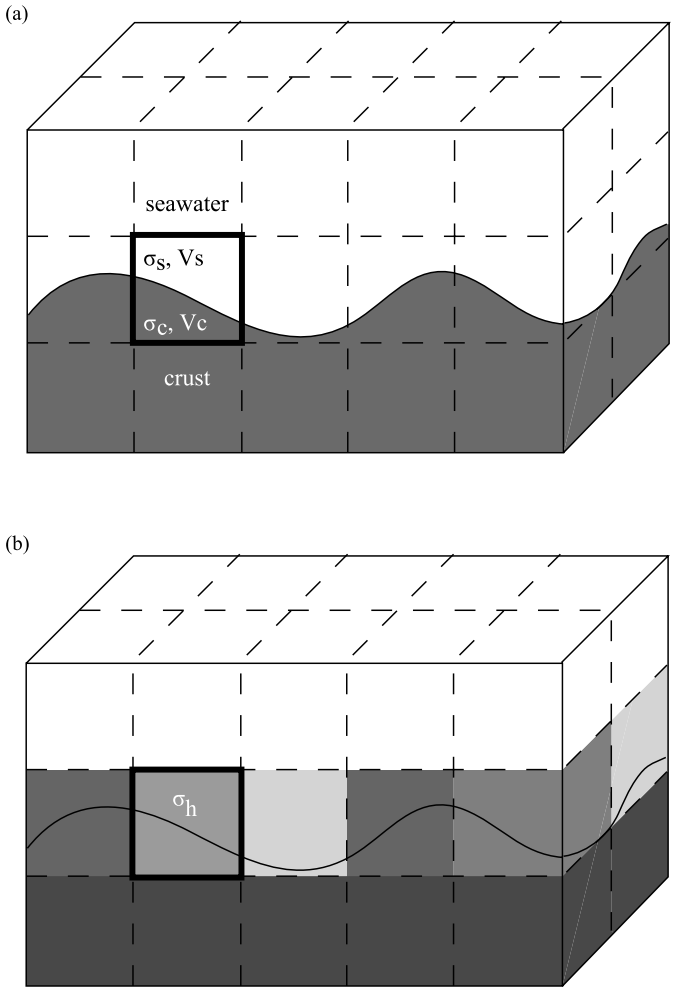

Fig. 1. Principle behind the incorporation of seafloor topography. (a) Example topography in rectangular blocks for numerical modeling. Seawater (white region) and crustal rock (dark region) have constant electrical conductivities σ_s and σ_c, and volumes V_s and V_c, respectively in the bold block. (b) The conductivities of the blocks that include both seawater and crustal rock portions, like the bold block, are calculated by conserving horizontal conductance within each block. For example, the conductivity of the bold block is calculated using Eq. (2) and is estimated to be σ_h.

km) with amplitudes of only a few kilometers. We can generally expect more accurate solutions by using the incorporation approach described in Li *et al*. (2008), because inversion solutions obtained using the correction approach depend on the accuracy of the approximation of the subseafloor structure. It is, however, neither efficient nor practical to incorporate topographic variations into one forward calculation using finer grid cells, especially when focusing on heterogeneous conductivity structures in the oceanic upper mantle and deeper parts with that are typically on a scale of 100 km or more both in the horizontal and vertical directions.

The aim of this paper is to propose an approximate treatment of topography that can be incorporated into 3-D seafloor MT inversion codes to study regional-scale mantle structure. In this study, new techniques are incorporated into the 3-D inversion code, WSINV3DMT (Siripunvaraporn *et al*., 2005), which is, at present, one of the practical inversions applied to land MT data.

We introduce a general treatment for incorporating topography and bathymetry into the model in Section 2. In Section 3, methods for calculating MT responses at arbitrary points on the undulating seafloor are introduced. The accuracy of the methods described in Sections 2 and 3 is tested in Section 4. In Section 5, a method for calculating sensitivity during inversion is derived. Finally, we apply the method to three kinds of synthetic datasets to verify its performance and then discuss the results in Section 6.

2. Expression of Seafloor Topography

The present problem is how to accurately express seafloor topography (the conductivity boundary) without significantly increasing the computational burden. To avoid using fine grids in the vertical direction, we propose applying a volumetric average of the conductivity for a block that includes the boundary (seafloor), as shown in Fig. 1. When fine topography is available in each block with a horizontal areal resolution of ΔS, the average conductivity of the block is obtained to conserve the horizontal conductance

$$\bar{\sigma} = \frac{\sum \Delta S \int_{z_+}^{z_-} \sigma_{1\mathrm{D}}^{(i)}(z)dz}{V}. \qquad (1)$$

Here z_+ and z_- are the top and bottom depths of the block, respectively, $\sigma_{1\mathrm{D}}^{(i)}(z)$ is the 1-D profile of the ith column, and V is the total volume of the block. If the conductivities

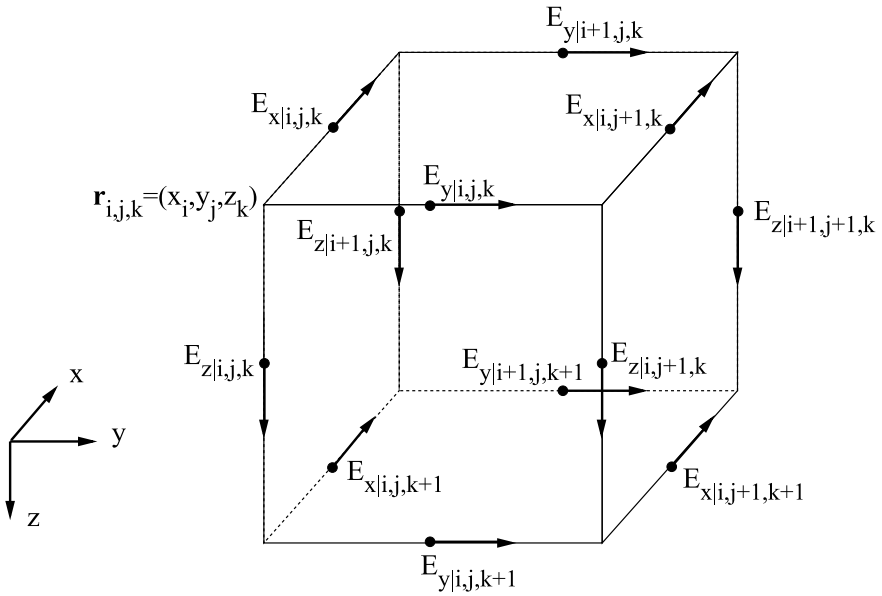

Fig. 2. Electric field components defined on a three-dimensional staggered grid.

of seawater and crust are both assumed to be uniform, the average electrical conductivity σ_h in a block including the seafloor can be calculated as

$$\sigma_h = \frac{\sigma_s V_s + \sigma_c V_c}{V_s + V_c}, \tag{2}$$

where σ_s and σ_c are the electrical conductivities of seawater and crustal rock, and V_s and V_c are the volumes occupied by seawater and crust in the block, respectively. This treatment allows us to easily design a mesh, regardless of the seafloor topography. It also does not increase the number of blocks in the vertical direction, thus restraining the number of model parameters, which is essential for compact forward calculation and for practical 3-D inversion.

The horizontal length scale of the topography included in a model is dependent on its horizontal mesh dimensions, which are usually set to be fine enough to resolve the observation arrays and target structure. Topography with a length scale larger than the horizontal mesh, and having various amplitudes, is efficiently incorporated by the method proposed above. If smaller scale topographic changes exist and their effect is not negligible, we have to divide the horizontal mesh into a finer grid although it increases computational costs. The alternative is an indirect approach, in which such small-scale topographic effects are treated separately and removed from observed EM responses as has been done, for example, by Baba and Chave (2005) for 2-D target structures. Hereinafter, we assume that the responses input to our 3-D inversions are free from the effects of small-scale topography, either because the effect is separately corrected or because it is negligible.

3. Calculation of MT Responses at Arbitrary Points

When we make forward calculations using coarse grids, the location of an observation site does not necessarily coincide with a grid point or an edge. We propose to calculate electromagnetic fields to estimate theoretical MT responses at each observation site using spatial interpolation and extrapolation. The mathematical formulation is described in this section, and its accuracy is tested in the next section.

In the forward calculations done in the WSINV3DMT, a second-order Maxwell's equation is solved for the electric field assuming time dependence $e^{-i\omega t}$ as

$$\nabla \times \nabla \times \mathbf{E}(\omega; \mathbf{r}) = i\omega\mu\sigma\mathbf{E}(\omega; \mathbf{r}), \quad \mathbf{r} = (x, y, z), \tag{3}$$

where μ is the magnetic permeability, ω is the angular frequency ($\omega = 2\pi/T$; T is the period), σ is the conductivity, and $\mathbf{E}(\omega; \mathbf{r}) = \begin{cases} E_x(\omega; \mathbf{r}) \\ E_y(\omega; \mathbf{r}) \\ E_z(\omega; \mathbf{r}) \end{cases}$ is the electric field at frequency ω and position $\mathbf{r}$. The dependence of the EM field on ω and $\mathbf{r}$ is sometimes treated as implicit in the equations that follow. With a staggered grid finite difference numerical approximation to (3), we obtain the discrete system of equations

$$\mathbf{AE} = \mathbf{b}. \tag{4}$$

Where $\mathbf{b} = \mathbf{b}(\omega; \mathbf{r})$ represent the posed boundary conditions for the electric field, and $\mathbf{A} = \mathbf{A}(\omega; \mathbf{r})$ are the symmetric coefficient matrix. For a model consisting of $N_x \times N_y \times N_z$ blocks, $\mathbf{b}$ is a column vector with $N_p = N_x \times (N_y+1) \times (N_z+1) + (N_x+1) \times N_y \times (N_z+1) + (N_x+1) \times (N_y+1) \times N_z$ elements and $\mathbf{A}$ is a $N_p \times N_p$ square complex matrix because the electric field defined at the edges of a block as shown in Fig. 2. The auxiliary fields (the magnetic field $\mathbf{H} = \mathbf{H}(\omega; \mathbf{r})$ in this case) are then computed directly from a first order Maxwell's equation or Faraday's law:

$$\nabla \times \mathbf{E} = i\omega\mu\mathbf{H}. \tag{5}$$

Two source polarizations, $E_x - H_y$ and $E_y - H_x$, are assumed, and (3) is solved via a forward modeling algo-

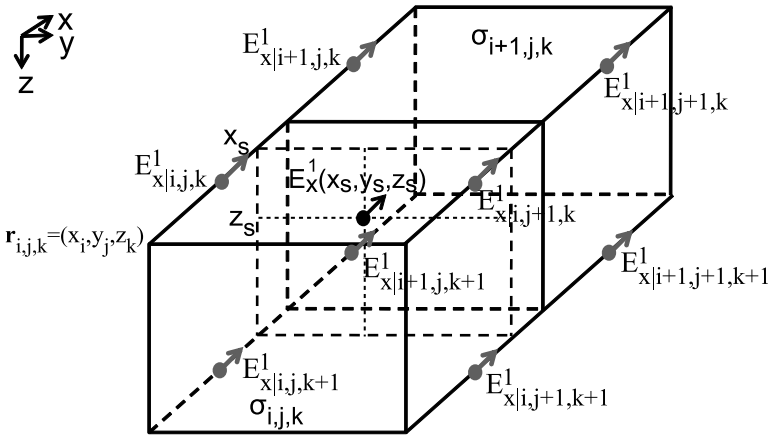

Fig. 3. Electric field components in the three-dimensional calculation blocks used for the MT impedance calculation. Gray arrows indicate electric field components on three-dimensional staggered grids. $E^1_x(x_s, y_s, z_s)$ is computed at an arbitrary point using eight electric fields at the block edges.

rithm to calculate the electric fields. The horizontal components of the fields from both polarizations are related by the impedance tensor $\mathbf{Z} = \mathbf{Z}(\omega; \mathbf{r})$

$$\begin{bmatrix} E^1_x & E^2_x \\ E^1_y & E^2_y \end{bmatrix} = \begin{bmatrix} Z_{xx} & Z_{xy} \\ Z_{yx} & Z_{yy} \end{bmatrix} \begin{bmatrix} H^1_x & H^2_x \\ H^1_y & H^2_y \end{bmatrix}. \tag{6}$$

Here E^1_x and E^2_x are the x-components of the electric field for the $E_x - H_y$ and $E_y - H_x$ source polarizations, respectively. The notation is similar for the other field components, so that the superscripts 1 and 2 denote the source polarization and the subscripts x and y denote components of the observed field, respectively.

On a staggered grid, the electric field components, $E_{x|i,j,k}$, $E_{y|i,j,k}$, and $E_{z|i,j,k}$, computed by solving (4) numerically, are defined at the centers of the edges of each block (Fig. 2), where $i = 1, \ldots, N_x$, $j = 1, \ldots, N_y$, and $k = 1, \ldots, N_z$ for $N_x \times N_y \times N_z$ blocks. The position of a grid node is denoted by $\mathbf{r}_{i,j,k} = (x_i, y_j, z_k)$ in a Cartesian coordinate system. The EM field components used for calculating the MT response at a site $\mathbf{r}_s = (x_s, y_s, z_s)$, where there may be an arbitrary point in a calculation block are computed by spatially interpolating the electric fields on the staggered grid:

$$\begin{aligned} E^p_x(\omega; \mathbf{r}_s) &= \mathbf{a}^T_p \mathbf{E}^p \\ E^p_y(\omega; \mathbf{r}_s) &= \mathbf{b}^T_p \mathbf{E}^p \\ H^p_x(\omega; \mathbf{r}_s) &= \mathbf{c}^T_p \mathbf{E}^p \\ H^p_y(\omega; \mathbf{r}_s) &= \mathbf{d}^T_p \mathbf{E}^p, \quad p = 1, 2. \end{aligned} \tag{7}$$

Here, $\mathbf{a}_{1,2}$, $\mathbf{b}_{1,2}$, $\mathbf{c}_{1,2}$, and $\mathbf{d}_{1,2}$ are vectors used to transform the electric fields on the staggered grid to the x- and y-components of the horizontal EM fields at the site for the first ($p = 1$) and second source ($p = 2$) polarizations. In this study, the site location on the seafloor can be at any arbitrary position within a block, not just on the block boundaries, because topography is expressed by converting the conductivity as described above. Consequently, the conversion should be considered in the calculation of the transform vectors.

The x- and y-components of the electric field at an MT site are obtained by interpolating eight electric field components on two blocks that surround the site (Fig. 3). For instance, $E^1_x(\omega; \mathbf{r}_s) = E^1_x(x_s, y_s, z_s)$ is calculated as follows.

$$\begin{aligned} &E^1_x\left(\frac{x_i + x_{i+1}}{2}, y_s, z_s\right) \\ &= \left\{ \frac{y_{j+1} - y_s}{y_{j+1} - y_j} E^1_{x|i,j,k} + \frac{y_s - y_j}{y_{j+1} - y_j} E^1_{x|i,j+1,k} \right\} \frac{z_{k+1} - z_s}{z_{k+1} - z_k} \\ &\quad + \left\{ \frac{y_{j+1} - y_s}{y_{j+1} - y_j} E^1_{x|i,j,k+1} + \frac{y_s - y_j}{y_{j+1} - y_j} E^1_{x|i,j+1,k+1} \right\} \frac{z_s - z_k}{z_{k+1} - z_k} \\ &E^1_x\left(\frac{x_{i+1} + x_{i+2}}{2}, y_s, z_s\right) \\ &= \left\{ \frac{y_{j+1} - y_s}{y_{j+1} - y_j} E^1_{x|i+1,j,k} + \frac{y_s - y_j}{y_{j+1} - y_j} E^1_{x|i+1,j+1,k} \right\} \frac{z_{k+1} - z_s}{z_{k+1} - z_k} \\ &\quad + \left\{ \frac{y_{j+1} - y_s}{y_{j+1} - y_j} E^1_{x|i+1,j,k+1} + \frac{y_s - y_j}{y_{j+1} - y_j} E^1_{x|i+1,j+1,k+1} \right\} \frac{z_s - z_k}{z_{k+1} - z_k}. \end{aligned} \tag{8, 9}$$

When the seafloor at the observation site is not flat, there are averaged conductivity contrasts between the calculation blocks because of lateral bathymetry variations. Thus, the interpolation is performed using electric current components calculated by Ohm's law because the normal component of the electric current should be continuous across the boundaries.

$$j_x\left(\frac{x_i + x_{i+1}}{2}, y_s, z_s\right) = E^1_x\left(\frac{x_i + x_{i+1}}{2}, y_s, z_s\right) \sigma_{i,j,k} \tag{10}$$

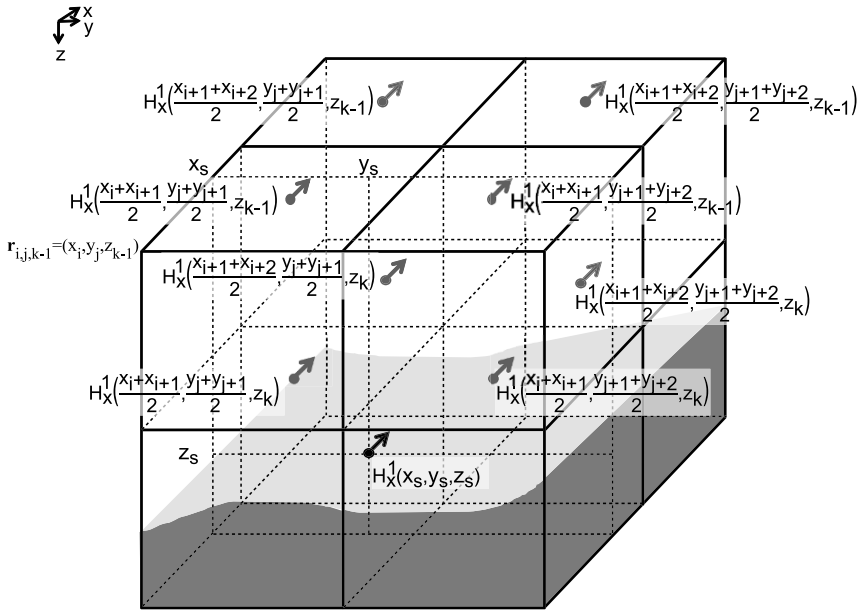

Fig. 4. Magnetic field components in the three-dimensional calculation blocks used for the MT impedance calculation. $H_x^1(x_s, y_s, z_s)$ is computed at an arbitrary point using the eight magnetic field components denoted by gray arrows at the centers of the block surfaces.

$$j_x\left(\frac{x_{i+1}+x_{i+2}}{2}, y_s, z_s\right) = E_x^1\left(\frac{x_{i+1}+x_{i+2}}{2}, y_s, z_s\right)\sigma_{i+1,j,k} \tag{11}$$

$$j_x(x_s, y_s, z_s) = \frac{x_{i+2}+x_{i+1}-2x_s}{x_{i+2}-x_i} j_x\left(\frac{x_i+x_{i+1}}{2}, y_s, z_s\right) + \frac{2x_s-x_i-x_{i+1}}{x_{i+2}-x_i} \times j_x\left(\frac{x_{i+1}+x_{i+2}}{2}, y_s, z_s\right). \tag{12}$$

Thus, we have

$$E_x^1(x_s, y_s, z_s) = j_x(x_s, y_s, z_s)/\sigma(x_s, y_s, z_s). \tag{13}$$

In the equations above, $E^1_{x|i,j,k}$, $E^1_{x|i+1,j,k}$, $E^1_{x|i,j+1,k}$, $E^1_{x|i+1,j+1,k}$, $E^1_{x|i,j,k+1}$, $E^1_{x|i+1,j,k+1}$, $E^1_{x|i,j+1,k+1}$, and $E^1_{x|i+1,j+1,k+1}$ are electric field components on the staggered grids. The first four of these components are in the seawater, and the others are in the seabed. $E_x^1(\frac{x_i+x_{i+1}}{2}, y_s, z_s)$ and $E_x^1(\frac{x_{i+1}+x_{i+2}}{2}, y_s, z_s)$ are calculated by bi-linearly interpolating the electric field components on the staggered grids ((8) and (9)). $j_x(\frac{x_i+x_{i+1}}{2}, y_s, z_s)$ and $j_x(\frac{x_{i+1}+x_{i+2}}{2}, y_s, z_s)$ are converted respectively from $E_x^1(\frac{x_i+x_{i+1}}{2}, y_s, z_s)$ and $E_x^1(\frac{x_{i+1}+x_{i+2}}{2}, y_s, z_s)$ using Ohm's law ((10) and (11)). $\sigma_{i,j,k}$ is the conductivity of a block, and $\sigma(x_s, y_s, z_s)$ is the conductivity of the block at the observation site, i.e., $\sigma(x_s, y_s, z_s) = \sigma_{i,j,k}$ if $\frac{x_i+x_{i+1}}{2} \le x_s < x_{i+1}$, while $\sigma(x_s, y_s, z_s) = \sigma_{i+1,j,k}$ if $x_{i+1} \le x_s < \frac{x_{i+1}+x_{i+2}}{2}$. The coefficients of the electric field components are included in the transform vector $\mathbf{a}_1^T$. The transform vectors $\mathbf{a}_2^T$ for $E_x^2(x_s, y_s, z_s)$, $\mathbf{b}_1^T$ for $E_y^1(x_s, y_s, z_s)$, and $\mathbf{b}_2^T$ for $E_y^2(x_s, y_s, z_s)$ are calculated in the same manner as for $E_x^1(x_s, y_s, z_s)$. Two blocks adjacent to each other in the y-direction area used to calculate $E_y^1(x_s, y_s, z_s)$ and $E_y^2(x_s, y_s, z_s)$.

The magnetic field at the MT site is calculated as follows. Here an example is shown for the case of the x-component for the first polarization, and the coefficients of $\mathbf{E}^1$ constitute $\mathbf{c}_1^T$. For observation sites on the seafloor, the magnetic field, $H_x^1(\omega; \mathbf{r}_s) = H_x^1(x_s, y_s, z_s)$, used to calculate the MT response is computed from the x-components of the magnetic field at eight points in the seawater, $H_x^1(\frac{x_i+x_{i+1}}{2}, \frac{y_j+y_{j+1}}{2}, z_k)$, $H_x^1(\frac{x_i+x_{i+1}}{2}, \frac{y_{j+1}+y_{j+2}}{2}, z_k)$, $H_x^1(\frac{x_{i+1}+x_{i+2}}{2}, \frac{y_j+y_{j+1}}{2}, z_k)$, $H_x^1(\frac{x_{i+1}+x_{i+2}}{2}, \frac{y_{j+1}+y_{j+2}}{2}, z_k)$, $H_x^1(\frac{x_i+x_{i+1}}{2}, \frac{y_j+y_{j+1}}{2}, z_{k-1})$, $H_x^1(\frac{x_i+x_{i+1}}{2}, \frac{y_{j+1}+y_{j+2}}{2}, z_{k-1})$, $H_x^1(\frac{x_{i+1}+x_{i+2}}{2}, \frac{y_j+y_{j+1}}{2}, z_{k-1})$, and $H_x^1(\frac{x_{i+1}+x_{i+2}}{2}, \frac{y_{j+1}+y_{j+2}}{2}, z_{k-1})$, as illustrated by the gray arrows in Fig. 4. Each magnetic component at the center of the top/bottom surface of each block is computed using Ampere's and Faraday's laws and 24 electric fields on the staggered grids as shown in Appendix A. First, four magnetic field components are linearly interpolated in the horizontal directions at each level as

$$\begin{aligned} &H_x^1(x_s, y_s, z_k) \\ &= \frac{x_{i+2}+x_{i+1}-2x_s}{x_{i+2}-x_i}\left\{\frac{y_{j+2}+y_{j+1}-2y_s}{y_{j+2}-y_j} \times H_x^1\left(\frac{x_i+x_{i+1}}{2}, \frac{y_j+y_{j+1}}{2}, z_k\right) + \frac{2y_s-y_{j+1}-y_j}{y_{j+2}-y_j} H_x^1\left(\frac{x_i+x_{i+1}}{2}, \frac{y_{j+1}+y_{j+2}}{2}, z_k\right)\right\} \\ &+ \frac{2x_s-x_{i+1}-x_i}{x_{i+2}-x_i}\left\{\frac{y_{j+2}+y_{j+1}-2y_s}{y_{j+2}-y_j} \times H_x^1\left(\frac{x_{i+1}+x_{i+2}}{2}, \frac{y_j+y_{j+1}}{2}, z_k\right) + \frac{2y_s-y_{j+1}-y_j}{y_{j+2}-y_j} H_x^1\left(\frac{x_{i+1}+x_{i+2}}{2}, \frac{y_{j+1}+y_{j+2}}{2}, z_k\right)\right\} \end{aligned} \tag{14}$$

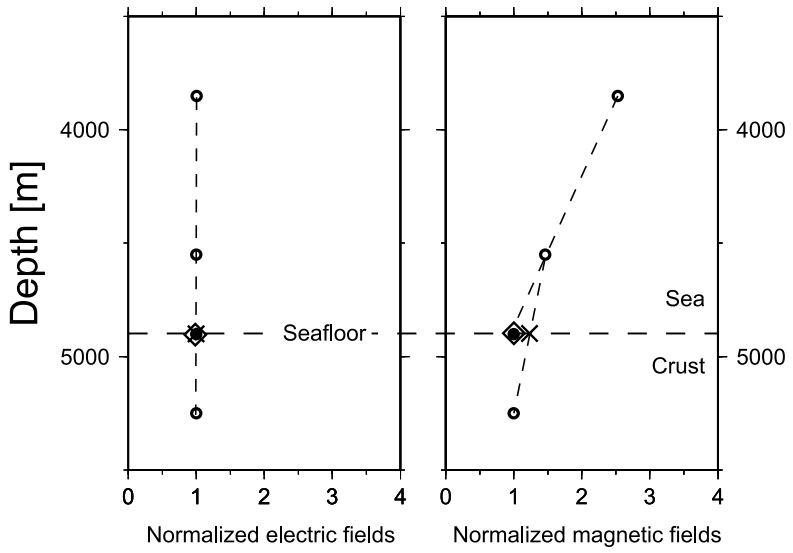

Fig. 5. $|E|$ and $|H|$ normalized by seafloor values versus depth for $T = 3000$. Open circles indicate the values of the EM field components calculated on the top/bottom surfaces of the blocks. Solid circles indicate the values of the EM field components on the seafloor, which is just bounded by the block surface when using mesh A. Diamonds and crosses indicate the values of the EM field components on the seafloor calculated by extrapolation and interpolation, respectively, using mesh B.

$$
\begin{aligned}
&H_x^1(x_s, y_s, z_{k-1}) \\
&= \frac{x_{i+2} + x_{i+1} - 2x_s}{x_{i+2} - x_i} \left\{ \frac{y_{j+2} + y_{j+1} - 2y_s}{y_{j+2} - y_j} \right. \\
&\times H_x^1\left(\frac{x_i + x_{i+1}}{2}, \frac{y_j + y_{j+1}}{2}, z_{k-1}\right) \\
&\left. + \frac{2y_s - y_{j+1} - y_j}{y_{j+2} - y_j} H_x^1\left(\frac{x_i + x_{i+1}}{2}, \frac{y_{j+1} + y_{j+2}}{2}, z_{k-1}\right) \right\} \\
&+ \frac{2x_s - x_{i+1} - x_i}{x_{i+2} - x_i} \left\{ \frac{y_{j+2} + y_{j+1} - 2y_s}{y_{j+2} - y_j} \right. \\
&\times H_x^1\left(\frac{x_{i+1} + x_{i+2}}{2}, \frac{y_j + y_{j+1}}{2}, z_{k-1}\right) \\
&+ \frac{2y_s - y_{j+1} - y_j}{y_{j+2} - y_j} \\
&\left. \times H_x^1\left(\frac{x_{i+1} + x_{i+2}}{2}, \frac{y_{j+1} + y_{j+2}}{2}, z_{k-1}\right) \right\}. \qquad (15)
\end{aligned}
$$

Then, $H_x^1(x_s, y_s, z_k)$ and $H_x^1(x_s, y_s, z_{k-1})$ are linearly extrapolated in the vertical direction as

$$
\begin{aligned}
H_x^1(x_s, y_s, z_s) = &\frac{z_s - z_{k-1}}{z_k - z_{k-1}} H_x^1(x_s, y_s, z_k) \\
&- \frac{z_s - z_k}{z_k - z_{k-1}} H_x^1(x_s, y_s, z_{k-1}). \qquad (16)
\end{aligned}
$$

$H_x^2(x_s, y_s, z_s)$, $H_y^1(x_s, y_s, z_s)$, and $H_y^2(x_s, y_s, z_s)$ are calculated in the same manner as $H_x^1(x_s, y_s, z_s)$. $\mathbf{c}_{1,2}$ and $\mathbf{d}_{1,2}$ are based on the above calculations.

The horizontal EM field components at an arbitrary point in a block are calculated based on linear interpolation of the components surrounding the point, as described above. The only exception is the magnetic field in the vertical direction, which we extrapolate. Figure 5 shows the vertical variations in the horizontal EM field components normalized by each value on the seafloor for a period of 3000 seconds. They are simulated by a 1-D conductivity model consisting of a seawater layer (3.2 S m^{-1}) and a half-space (0.01 S m^{-1}). The EM field is simulated using two mesh designs. In the first (A), the seafloor is just bounded by the block interface. In the second mesh design (B), the seafloor is located within a block. The block size in the vertical direction is 700 m. The conductivity of the block is obtained from (2), and the horizontal EM field components on the seafloor are calculated using the approximating treatment. Solid circles indicate the EM field component values on the seafloor obtained using mesh A. Diamonds and crosses indicate the EM field component values on the seafloor calculated by extrapolating and interpolating, respectively, the values given by the black circles, using mesh B. For the electric field, the diamond and cross both agree well with the solid circle. This is because the attenuation of the horizontal electric field with depth is smaller than that of the magnetic field. For the magnetic field, the diamond is nearly identical to the solid circle, but the cross is significantly different, as can be expected from the difference in conductivity between the seawater and crust. This contrast causes a discontinuity in the vertical gradient of the horizontal magnetic field at the seafloor by (5). Thus, the interpolation produces a large error when mesh B is used. Because of this, we adopted the extrapolation method for calculating the horizontal magnetic field components at MT sites. We extrapolate from above the seafloor because the conductivity of seawater is fixed as a known parameter throughout the inversion process.

This approximate treatment of topography (hereinafter called ATT) includes expressing the ocean bottom conductivity by volumetric averaging and using interpolation and extrapolation methods to calculate the EM fields at arbitrary observation sites.

4. Synthetic Test of the Accuracy of Forward Calculations Using ATT

We tested the accuracy of MT responses calculated using the WSINV3DMT with ATT by comparing them with

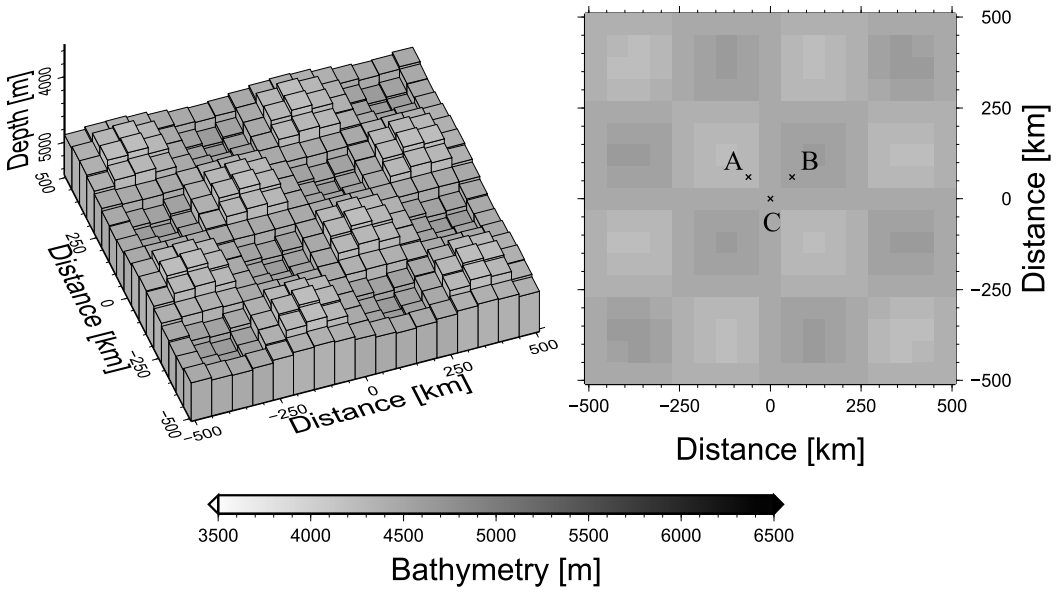

Fig. 6. Three-dimensional view (left) and plan view (right) of the synthetic seafloor topography model. The crosses with labels are the positions where synthetic MT responses were calculated. Sites A, B, and C are located on the flank of a seamount, on the flank of a dip, and on the flank between two seamounts and two dips, respectively.

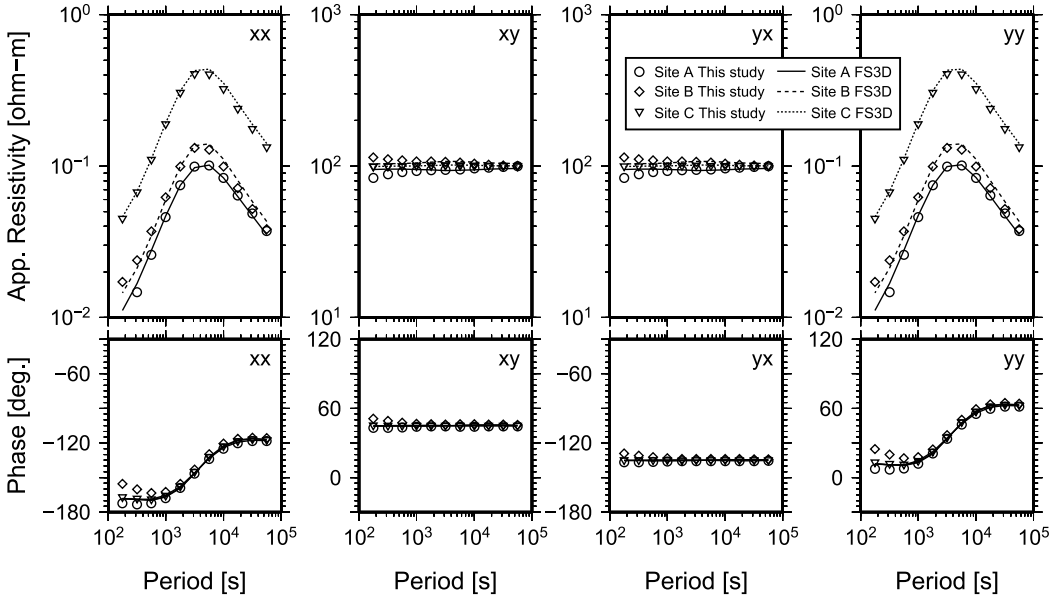

Fig. 7. Synthetic apparent resistivity and phase at the three locations shown in Fig. 6. Circles, diamonds, and triangles show the responses calculated by the forward part of the WSINV3DMT with approximate treatment of topography (ATT) for sites A, B, and C, respectively. Solid, broken, and dotted lines are the responses calculated by the FS3D algorithm (Baba and Seama, 2002) for sites A, B, and C, respectively.

responses calculated using the FS3D algorithm (Baba and Seama, 2002) and a synthetic seafloor topography model over a 0.01 S m^{-1} half-space (Fig. 6). The horizontal discretizations used for the WSINV3DMT with ATT and the FS3D algorithm were the same, while the mesh size in the vertical direction for the WSINV3DMT with ATT model was half of the mesh size for the FS3D algorithm. The WSINV3DMT with ATT model applies the volumetric average of the conductivity for blocks including the seafloor, and MT responses are calculated at the depths where the seafloor lies in the blocks, while the FS3D method converts the topographic change into changes in electrical conductivity and magnetic permeability in two layers bounding a flattened seafloor so that MT responses are calculated on block surfaces that express the flattened seafloor (Baba and Seama, 2002). The synthetic seafloor topography is described by

$$\begin{aligned}&\mathrm{Depth}(x, y)\\&= 4900 + 250\sin(2\pi x/500000)\sin(2\pi y/500000),\end{aligned} \quad (17)$$

where the unit of length is meter. The topography model is discretized every 60 km in the horizontal directions. We calculated MT responses for 11 periods (from 177 to 56,234 seconds) at three points: Site A is located on the flank of a seamount, site B on the flank of a dip, and site C on the

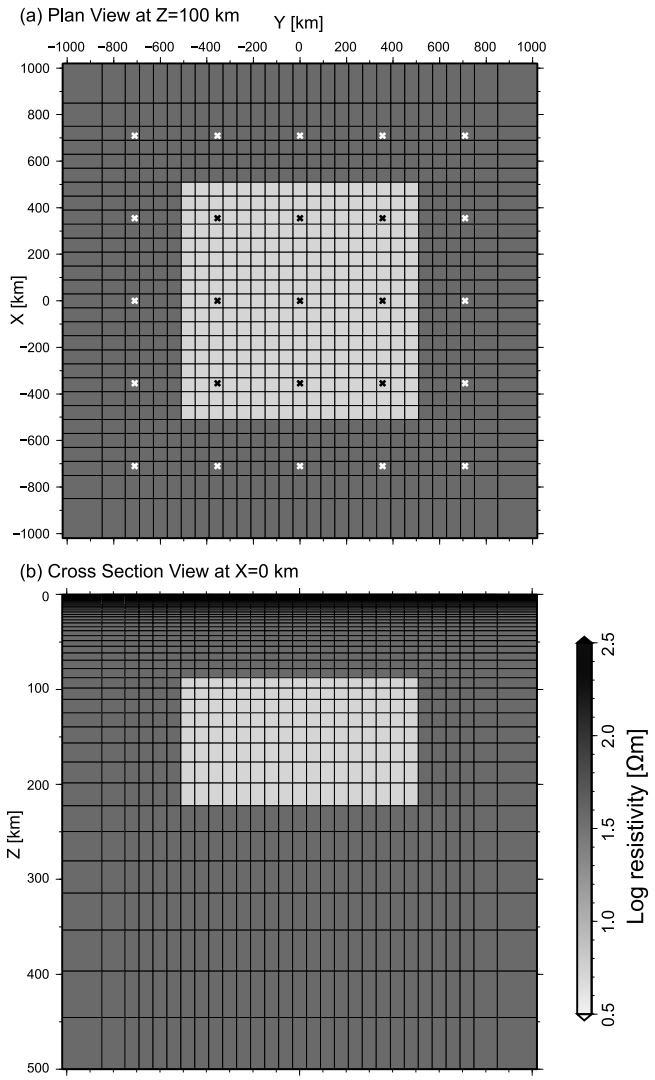

Fig. 8. Synthetic model for Case I. (a) Plan view at $z = 100$ km and (b) cross-section at $x = 0$ km. The seafloor is flat in this model. Crosses indicate the site locations.

flank between two seamounts and two dips. The calculated apparent resistivities and phases are plotted in Fig. 7. The amplitudes of the diagonal components of the impedance tensor are only produced by topographic variations in this test because the conductivity below the seafloor is assumed to be constant and therefore the values of the diagonal elements should be zero when the seafloor is flat. The responses from the two calculations agree within 0.04 on a logarithmic scale of apparent resistivity and 2.9 degrees in the phase of the off-diagonal components, particularly for periods longer than 500 seconds. MT responses at shorter periods show less agreement than those at longer periods since shorter periods are more influenced by the differences between the topographic treatments because the volumetric averaging approximation used in the ATT is less accurate for shorter periods. Although more accurate results can be expected using finer meshes in the vertical direction, in exchange for increased computational cost, this limitation for short periods is not serious, because real marine data deeper than about 5000 m below sea level usually provide good MT responses at periods longer than 500 seconds (Baba *et al.*, 2010). The relatively low accuracy of diagonal elements will not cause a serious problem because their amplitudes are much smaller than those of the off-diagonal elements. In addition, the observation errors in the diagonal elements are typically of the same order as in the off-diagonal elements, and much larger than the differences in Fig. 7. If a 3% relative numerical error is acceptable, one can use MT responses for periods longer than 500 s. If a 10% relative numerical error can be accepted, MT responses at all periods longer than 100 s may be used for inversion. Otherwise, a finer mesh in the vertical direction can be used to get more accurate results, but with increased computational costs. Therefore, we may conclude that incorporating the ATT in the forward calculation of the WSINV3DMT is accurate enough for 3-D inversion.

5. Calculation of Sensitivity

The ATT process described above must also be applied to calculate sensitivities in order to be effective in inversion. Sensitivity is a measure of the amount of change in the MT impedances caused by variations in a model parameter (the log of the electrical resistivity). According to Newman and Alumbaugh (2000), for the kth model parameter m_k,

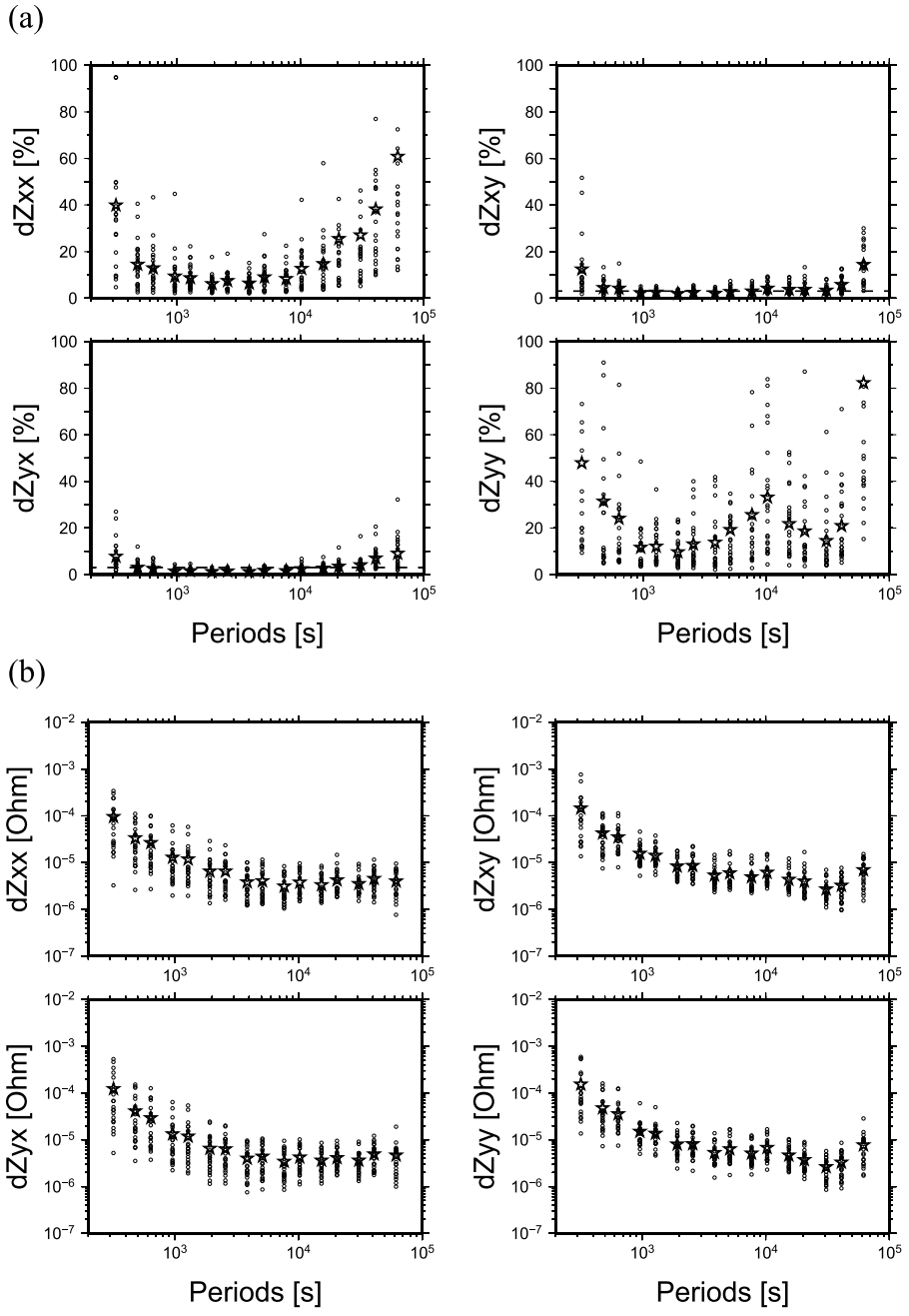

Fig. 9. (a) Relative errors of real MT responses obtained from 25 ocean bottom electromagnetometers (OBEMs) deployed in and around the Philippine Sea (Baba *et al.*, 2010). Circles and stars indicate the errors for each OBEM's data and their averages, respectively. Dashed lines in the xy- and yx-components indicate 3% error levels. (b) Absolute errors of the MT responses. Circles and stars indicate the errors for the OBEM data and their averages, respectively.

components of the sensitivity for each site in each period are

$$\frac{\partial Z_{xx}(\omega;\mathbf{r}_s)}{\partial m_k} = \mathbf{g}^1_{xx}(\omega;\mathbf{r}_s)^T \frac{\partial \mathbf{E}^1}{\partial m_k} + \mathbf{g}^2_{xx}(\omega;\mathbf{r}_s)^T \frac{\partial \mathbf{E}^2}{\partial m_k} + \frac{\partial \mathbf{g}^1_{xx}(\omega;\mathbf{r}_s)^T}{\partial m_k}\mathbf{E}^1 + \frac{\partial \mathbf{g}^2_{xx}(\omega;\mathbf{r}_s)^T}{\partial m_k}\mathbf{E}^2,$$

$$\frac{\partial Z_{xy}(\omega;\mathbf{r}_s)}{\partial m_k} = \mathbf{g}^1_{xy}(\omega;\mathbf{r}_s)^T \frac{\partial \mathbf{E}^1}{\partial m_k} + \mathbf{g}^2_{xy}(\omega;\mathbf{r}_s)^T \frac{\partial \mathbf{E}^2}{\partial m_k} + \frac{\partial \mathbf{g}^1_{xy}(\omega;\mathbf{r}_s)^T}{\partial m_k}\mathbf{E}^1 + \frac{\partial \mathbf{g}^2_{xy}(\omega;\mathbf{r}_s)^T}{\partial m_k}\mathbf{E}^2,$$

$$\frac{\partial Z_{yx}(\omega;\mathbf{r}_s)}{\partial m_k} = \mathbf{g}^1_{yx}(\omega;\mathbf{r}_s)^T \frac{\partial \mathbf{E}^1}{\partial m_k} + \mathbf{g}^2_{yx}(\omega;\mathbf{r}_s)^T \frac{\partial \mathbf{E}^2}{\partial m_k} + \frac{\partial \mathbf{g}^1_{yx}(\omega;\mathbf{r}_s)^T}{\partial m_k}\mathbf{E}^1 + \frac{\partial \mathbf{g}^2_{yx}(\omega;\mathbf{r}_s)^T}{\partial m_k}\mathbf{E}^2,$$

$$\frac{\partial Z_{yy}(\omega;\mathbf{r}_s)}{\partial m_k} = \mathbf{g}^1_{yy}(\omega;\mathbf{r}_s)^T \frac{\partial \mathbf{E}^1}{\partial m_k} + \mathbf{g}^2_{yy}(\omega;\mathbf{r}_s)^T \frac{\partial \mathbf{E}^2}{\partial m_k} + \frac{\partial \mathbf{g}^1_{yy}(\omega;\mathbf{r}_s)^T}{\partial m_k}\mathbf{E}^1 + \frac{\partial \mathbf{g}^2_{yy}(\omega;\mathbf{r}_s)^T}{\partial m_k}\mathbf{E}^2. \tag{18}$$

The electric fields, $\mathbf{E}^1$ and $\mathbf{E}^2$, in (18) are the forward solutions of (4) for the first and second source polarizations.

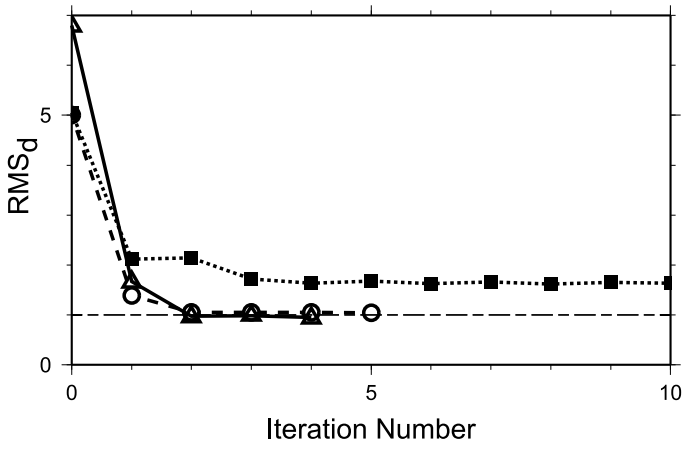

Fig. 10. RMS_d misfit versus iteration number for the three inversions of the synthetic data. Triangles, circles, and squares are for Case I, Case II, and Case III, respectively.

For simplicity, the dependence of impedance and the eight vectors $\mathbf{g}^1_{xx}$, $\mathbf{g}^2_{xx}$, $\mathbf{g}^1_{xy}$, $\mathbf{g}^2_{xy}$, $\mathbf{g}^1_{yx}$, $\mathbf{g}^2_{yx}$, $\mathbf{g}^1_{yy}$, and $\mathbf{g}^2_{yy}$ on ω and $\mathbf{r}$ is again treated as implicit in the equations that follow. The eight vectors are expressed by linear combinations of the transform vectors in (7) that interpolate the electric field components and interpolate and extrapolate the magnetic field components for the two source polarizations in the forward part. Combining the derivative of (4) with respect to the model parameter and (18), for the xx-component we have

$$\frac{\partial Z_{xx}}{\partial m_k} = -\mathbf{g}^{1\ T}_{xx}\mathbf{A}^{-1}\frac{\partial \mathbf{A}}{\partial m_k}\mathbf{E}^1 - \mathbf{g}^{2\ T}_{xx}\mathbf{A}^{-1}\frac{\partial \mathbf{A}}{\partial m_k}\mathbf{E}^2 + \frac{\partial \mathbf{g}^{1\ T}_{xx}}{\partial m_k}\mathbf{E}^1 + \frac{\partial \mathbf{g}^{2\ T}_{xx}}{\partial m_k}\mathbf{E}^2. \tag{19}$$

For example, $\mathbf{g}^1_{xx}$ in (19) can be written as

$$\mathbf{g}^1_{xx} = \frac{H^2_y(\mathbf{r}_s)\mathbf{a}^T_1 + (-E^2_x(\mathbf{r}_s) + Z_{xx}H^2_x(\mathbf{r}_s))\mathbf{d}^T_1 - Z_{xx}H^2_y(\mathbf{r}_s)\mathbf{c}^T_1}{H^1_x(\mathbf{r}_s)H^2_y(\mathbf{r}_s) - H^2_x(\mathbf{r}_s)H^1_y(\mathbf{r}_s)}. \tag{20}$$

Because $\mathbf{a}_1$ includes model parameters as shown in (8) to (13), (20) indicates that $\mathbf{g}^1_{xx}$ includes model parameters as shown in (8) to (13). The differences in the model parameters used in the eight vectors depend on the location of the calculated MT responses. We therefore have to use suitable model parameters for each site where MT responses are computed, so the sensitivities can be calculated accurately. For example, the conductivities of seven blocks, $\sigma_{i,j,k}$, $\sigma_{i,j+1,k}$, $\sigma_{i+1,j,k}$, $\sigma_{i,j,k-1}$, $\sigma_{i,j+1,k-1}$, $\sigma_{i+1,j,k-1}$, and $\sigma_{i+1,j+1,k-1}$, except for the top and right back block, are used when MT responses are computed at site $\mathbf{r}_s$ in Fig. 4. Here, $\frac{x_i+x_{i+1}}{2} \le x_s < x_{i+1}$, $\frac{y_j+y_{j+1}}{2} \le y_s < y_{j+1}$, and $z_k \le z_s < z_{k+1}$.

6. Synthetic Inversion and Discussion

Here the total performance of the WSINV3DMT with ATT was tested using three synthetic datasets. The three synthetic datasets were generated using the forward part of the WSINV3DMT with ATT code. The first dataset was calculated for a conductive block buried in a half-space below the ocean with constant water depth. The second was calculated for a conductive block buried in a half-space below the ocean with realistic topography, and the third was a checkerboard model below the ocean with realistic topography. All synthetic models were discretized every 60 km in the horizontal direction in the central part of the model domain. The vertical meshes were discretized every 700 m near the seafloor, and the length of the mesh increases exponentially with increasing depth. All the models included seven air layers in the default configuration, and the conductivity values of the seven air layers were fixed in all the inversion calculations. The number of observation sites is 25 where synthetic MT responses are computed.

6.1 Case I

The first example is a very simple model (Fig. 8), consisting of a conductive block of 0.1 S m^{-1} (1020 km × 1020 km × 135 km) buried at a depth of 80 km beneath a flat seafloor. The background structure is a 0.01 S m^{-1} half-space beneath a 4900-m-thick seawater layer with a conductivity of 3.2 S m^{-1}. The model consists of a $35 \times 35 \times 51$ (+ seven air layers) grid. Synthetic data containing 3% Gaussian noise were generated for 25 sites. The site locations are shown by the crosses in Fig. 8. We inverted all four elements of the complex impedance tensor Z_{xx}, Z_{xy}, Z_{yx}, and Z_{yy} for four periods (1000, 3000, 10,000, and 30,000 seconds). To provide the error bar for each impedance, we referred to error estimates for real observations from 25 ocean bottom magnetometers (OBEMs) deployed in the Philippine Sea (Baba *et al.*, 2010). As shown in Fig. 9(a), the relative (%) errors of the diagonal components were much larger than those of the off-diagonal components. However, the absolute values of the error bars were of similar magnitudes (Fig. 9(b)). Therefore in the synthetic tests, the errors in the diagonal components were calculated from the errors in the off-diagonal components of the observed impedance for each period as

$$\delta Z_{\mathrm{on}} = \delta Z_{\mathrm{off}} = \sqrt{\left(\frac{\delta Z_{xy}}{2}\right)^2 + \left(\frac{\delta Z_{yx}}{2}\right)^2}, \tag{21}$$

where δZ_{on}, δZ_{off}, δZ_{xy}, and δZ_{yx} are the average absolute errors (stars in Fig. 9(b)) of the diagonal, the off-diagonal, and the xy- and yx-components, respectively. The mesh de-

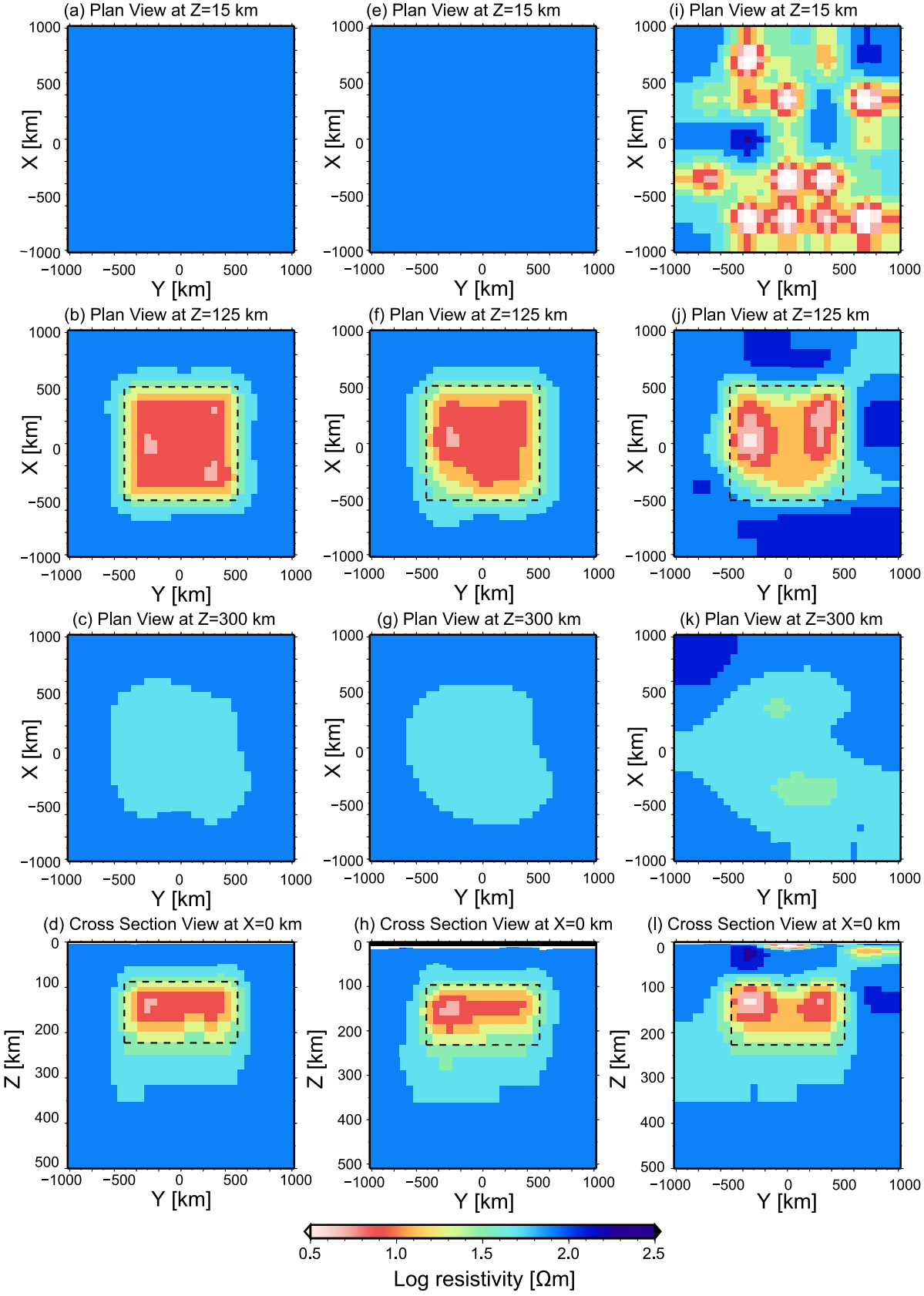

Fig. 11. Inverted models for Case I and Case II. The left ((a)–(d)), center ((e)–(h)), and right ((i)–(l)) panels show the models for Case I (fourth iteration, RMS_d misfit = 0.95), Case II (fifth iteration, RMS_d misfit = 1.04), and Case II using the wrong treatment of the topography (tenth iteration, RMS_d misfit = 3.47), respectively. The panels in the top three rows ((a)–(c), (e)–(g), and (i)–(k)) are plan views at 15, 125, and 300 km depth, and the bottom panels ((d), (h), and (l)) are cross-section views cutting across the anomalous body at $X = 0$ km. The black dashed lines indicate the outline of the synthetic conductive anomaly. The solutions are shown only in the central part of the model domain.

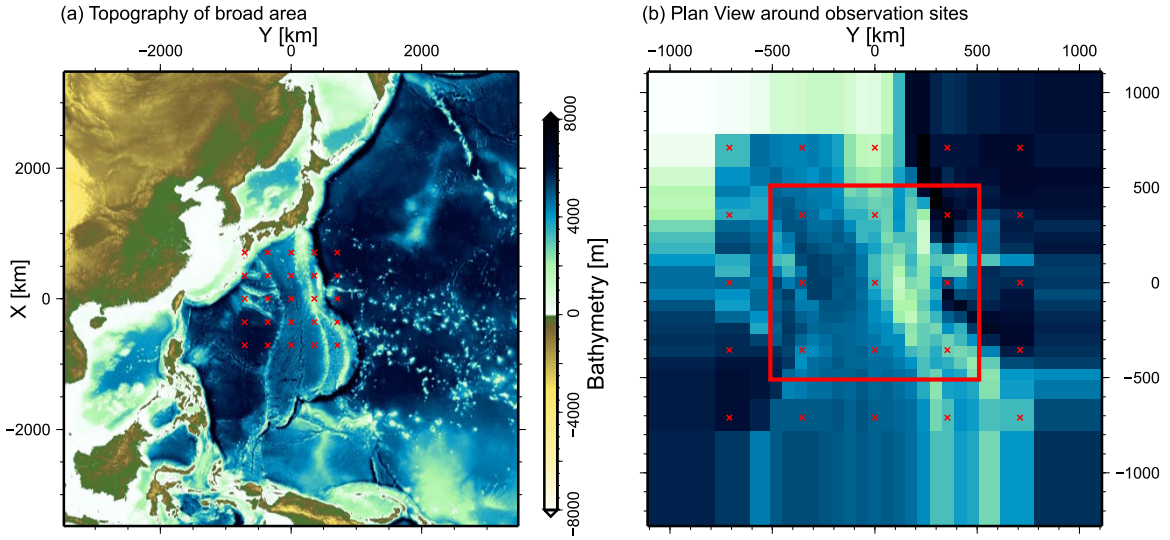

Fig. 12. (a) Bathymetric map of Case II. The map is created by real bathymetry (2′ mesh) data from Smith and Sandwell (1994). The red crosses indicate the sites where the synthetic MT responses were calculated. (b) Plan view of the synthetic model with bathymetry in the central area of the model. The red crosses indicate the observation sites, and the red square indicates the region of the anomalous body.

sign used for the synthetic inversion is the same as that used for the forward modeling. The seawater layer discretized by seven layers, and the conductivity of each block representing seawater is 3.2 S m^{-1} and is treated as a fixed parameter in the inversion. In this simple test, the total number of data points (N) is 800, and the total number of model parameters to be solved (M) is 53,900. The inversion started from an initial model consisting of a 0.01 S m^{-1} half-space below the flat seafloor, which was also used as the prior model (Siripunvaraporn *et al.*, 2005). The inversion code searches the model around this prior.

The root mean square misfit of the data (hereinafter called the RMS$_d$ misfit) was defined as

$$\mathrm{RMS}_d = \sqrt{\left(\sum_{i=1}^{N_d} \frac{|d_i - F[m]_i|^2}{\delta_i^2} \right) \Big/ N_d}, \qquad (22)$$

where N_d is the number of data points and δ is the error of the synthetic data. The RMS$_d$ misfits for all components of the inversion iteration are indicated by triangles in Fig. 10, and the fourth iteration of the inverted model is shown in Figs. 11(a)–(d). We set the target RMS$_d$ misfit at one, and the inversion converged at the fourth iteration with an RMS$_d$ misfit of 0.95. In this inversion, the goal is to find the minimum norm model subject to this RMS$_d$ (see details in Siripunvaraporn *et al.*, 2005). Figures 11(a)–(c) show the plan views at respective depths of 15 km, 125 km (including the anomalous body), and 300 km, while Fig. 11(d) shows a cross-section through the middle of the anomalous body at $X = 0$ km. Figures 11(a)–(d) show that the inversion recovered the conductivity and the position of the anomalous body with sufficient accuracy. The image is not perfect at the top and bottom of the anomalous body, primarily due to smoothness constraints in the inversion. However, the result indicates that the 3-D inversion is accurate enough if the seafloor is flat.

6.2 Case II

For the next step, we tested a case with complex bathymetry and realistic lateral variation. The model again consists of an anomalous block of 0.1 S m^{-1} (1020 km × 1020 km × 135 km) buried in a 0.01 S m^{-1} half-space 88 km depth beneath the sea surface with real topography (Fig. 12). Here, the topography data are on a 2′ grid obtained from Smith and Sandwell (1994). The 25 sites are distributed uniformly in 5 × 5 grids, as shown in Fig. 12. Synthetic data for periods of 1000, 3000, 10,000, and 30,000 seconds were generated and inverted, so $N = 800$. 3% Gaussian noise was added to the data. The model consists of 35, 35, and 69 blocks (including seven air layers on the top) in the x-, y-, and z-directions, respectively, and is the same as the forward modeling that generated the synthetic data. The initial model and the prior model for the inversion have a uniform conductivity beneath the seafloor, similar to Case I, i.e., a 0.01 S m^{-1} half-space. The conductivity of each block representing seawater (3.2 S m^{-1}), including the seafloor, or above the sea surface (air and/or land) is treated as a fixed parameter in the inversion, so that $M = 53446$. The number of layers above the seafloor is variable between 11 and 24, depending on bathymetry.

Circles show the convergence of the full components in Fig. 10, and the fifth iteration of the inverted model is shown in Figs. 11(e)–(h). The inversion converged at the fifth iteration with an RMS$_d$ misfit of 1.04. The target RMS$_d$ misfit was set at one as in Case I. The inversion recovers a reasonable image of the conductive body as shown in Figs. 11(e)–(h), though the recovery is not perfect, especially at greater depths. Again, we confirmed that the ATT technique can be applied to invert seafloor MT data without serious loss of accuracy.

In order to display the importance of a proper topographical treatment, we attempted another inversion test using the synthetic data from Case II. However in this test, we assumed *a priori* the seafloor to be flat with a constant depth of 5000 m, an average value for all 25 sites. This inversion

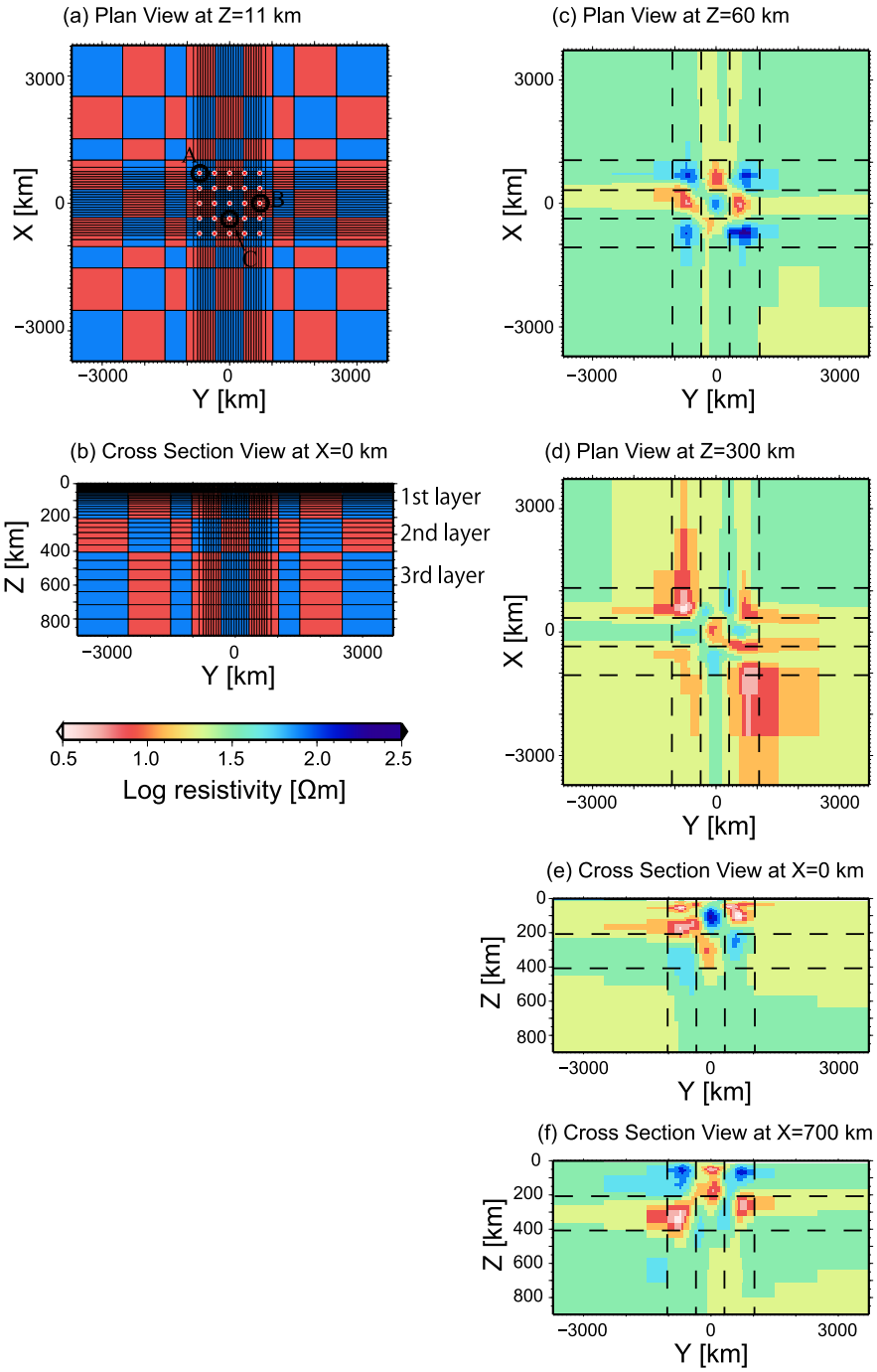

Fig. 13. Synthetic and inverted models for Case III (checkerboard test). Panels (a) and (b) are a plan view ($z = 11$ km) and cross-section ($x = 0$ km) of the synthetic model, respectively. The white crosses indicate the site locations. Panels (c)–(f) are the inverted model at the eighth iteration, with RMS_d misfit = 1.62. Panels (c) and (d) are plan views at 60 km and 300 km depth, and panels (e) and (f) are cross-sectional views cutting at $x = 0$ km and 700 km, respectively. The dashed lines denote the conductivity boundaries indicated in the synthetic models (a) and (b) and are only plotted in the central part of the model domain.

did not achieve the target RMS_d within ten iterations, and the minimum RMS_d was as large as 3.47 at the tenth iteration. The tenth iteration of the inverted model is shown in Figs. 11(i)–(l). The minimum RMS_d of this inversion is more than three times larger than that of the inversion using ATT (Case II). As shown in Fig. 11(j), the resulting image of the conductivity anomaly is divided into two anomalies lying between depths of 100 and 150 km. Both anomalies have much higher conductivity (0.21 S m^{-1}) than the given value (0.1 S m^{-1}). Furthermore, there are several false anomalies, especially in the shallower regions (Fig. 11(i)), producing extremely anomalous values exceeding 2.0 S m^{-1} or as low as 0.001 S m^{-1}. The results above indicate that an appropriate treatment of seafloor topography is definitely important in recovering an accurate conductivity model from marine MT data.

6.3 Case III

We also tested the inversion for a more complex model. This model consisted of blocks in a checkerboard pattern with alternating conductivity, 0.1 S m^{-1} and 0.01 S m^{-1},

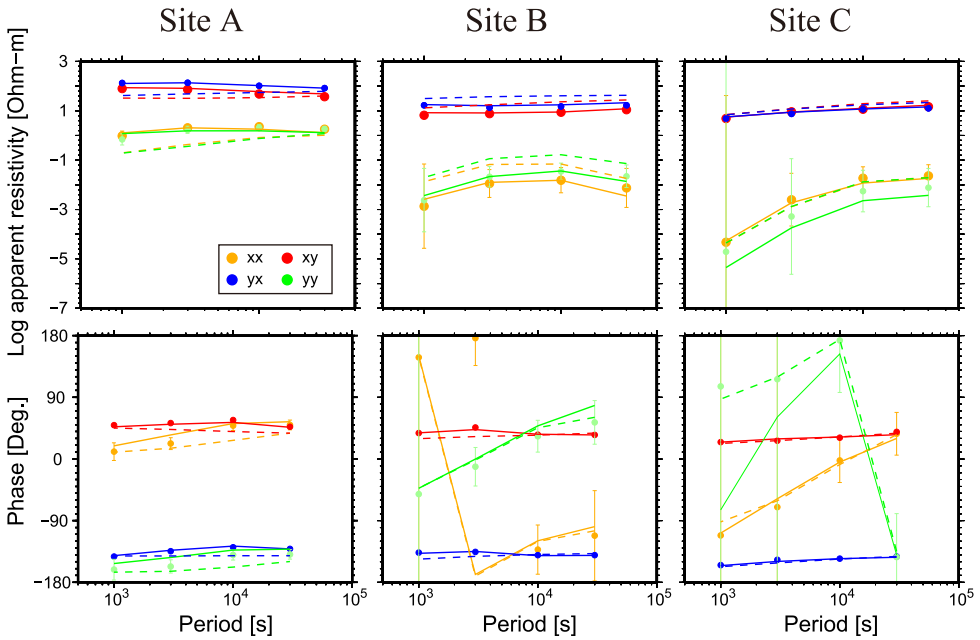

Fig. 14. Apparent resistivity and phase for the eighth iteration of the inverted model at sites A, B, and C, as indicated in Fig. 13(a). Dots show synthetic data, and dashed and solid lines show model responses of the starting model and inverted model (at the eighth iteration), respectively.

embedded in a 0.03 S m^{-1} half-space with real topography. Figures 13(a) and (b) show only the checkerboard part. The topography is the same as described in Fig. 12. Again, the initial and prior models are the same, 0.03 S m^{-1} half-spaces.

The convergence of the total RMS data misfit is indicated by squares in Fig. 10. It shows that the inversion reached a minimum RMS$_d$ misfit of about 1.62 at the eighth iteration, and remaining relatively constant thereafter. This RMS$_d$ is relatively high compared with those in the Case I and II. This is probably due to the checkerboard model because an inversion test to a flat seafloor over the same checkerboard structure reached a minimum RMS$_d$ misfit of about 1.77 after 10 iterations (not shown). The test was conducted on a supercomputer (SGI Altix 4700) at the Earthquake Research Institute, University of Tokyo, with an actual (wall clock) run time of about 10 minutes on 8 nodes for 10 iterations. Figure 14 shows the apparent resistivities and phases calculated from the initial model and from the eighth iteration of the inverted model for sites A, B, and C, as indicated in Fig. 13(a). The MT responses calculated in the eighth iteration fit the synthetic responses within the error bars, while a significant discrepancy is found between observed responses and those calculated for the initial model.

As shown in Figs. 13(c)–(f), the checkerboard patterns in the first and the second layers, 10–200 km and 200–400 km beneath the sea surface, respectively, were mostly recovered beneath the assumed MT sites, while the pattern in the third layer (400–900 km beneath the seawater) was not recovered well in this test. Figure 15 shows a model recovery (Zhang *et al.*, 2012), which indicates the differences in model parameters δm_k between the inverted (after i'th iteration) and the synthetic models so that

$$\delta m_{ik} = m_{ik}^{\mathrm{inv}} - m_k^{\mathrm{model}} \quad (k = 1, 2, \ldots, M). \tag{23}$$

White indicates that the inverted value of the block is close to the value in the synthetic model. Red and blue indicate that inverted values for these blocks are overestimated and underestimated, respectively. The edge of the conductive anomaly is colored red, while the edge of the resistive anomaly is blue. To evaluate the recovery of the conductivity structure, we calculated the RMS misfit between the synthetic model and the inverted model (RMS$_\sigma$ misfit), which can be defined as

$$\mathrm{RMS}_\sigma = \sqrt{\left\{\sum_{k=1}^{N_b} (\delta m_{ik})^2\right\} \Big/ N_b}, \tag{24}$$

where N_b is the number of blocks used for calculating the RMS$_\sigma$, and δm_{ik} is the model recovery (23). We focused on the RMS$_\sigma$ misfit within 1020 km from the origin in x- and y-directions. Note that the RMS$_\sigma$ misfit is 0.50 for the initial model because the conductivity of the initial model differs from the synthetic model by half an order of magnitude. At the eighth iteration, the first and second layers show RMS$_\sigma$ misfits of 0.40 and 0.45, respectively. However, the total RMS$_\sigma$ misfit value for the third layer is 0.52, suggesting that little improvement was attained in eight iterations, as shown in Figs. 13(e), (f), 15(c), and (d). In the first layer (Fig. 13(c)), the conductive and resistive regions have respective RMS$_\sigma$ values of 0.35 and 0.42 while in the second layer (Fig. 13(d)), the conductive and resistive regions have RMS$_\sigma$ values of 0.37 and 0.53. This implies that conductive anomalies can be detected more clearly than resistive ones. Generally a resistive region located vertically between conductive regions is difficult to resolve because induction occurs mostly in conductive regions. The checkerboard model is entirely symmetric, but the inverted model is not. Therefore, differences in the model resolution can be ascribed to the topography.

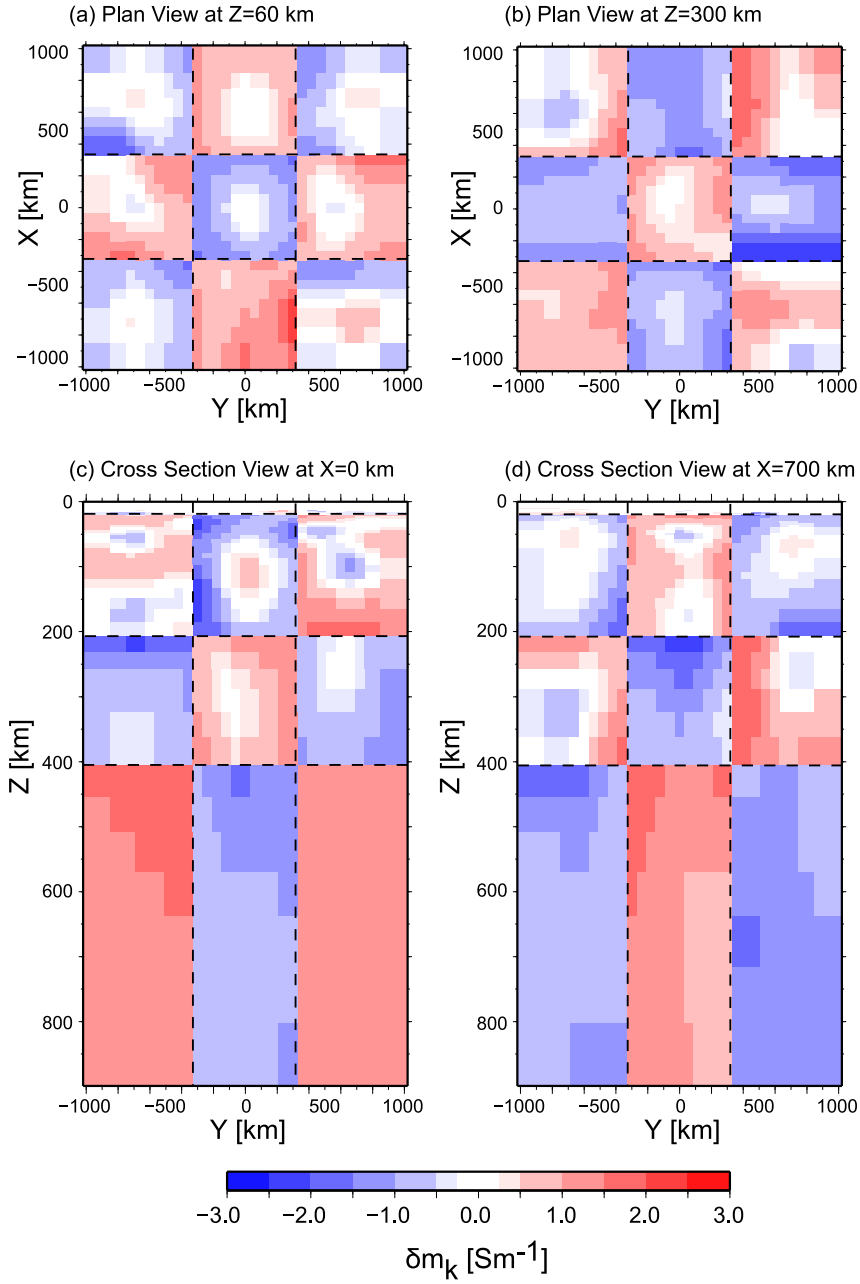

Fig. 15. Image of model recovery for Case III. These are only shown from the origin to 1200 km in the x- and y-directions. The black dashed lines denote the conductivity boundary indicated in the synthetic model (Fig. 13(a)).

7. Conclusions

In this study, we propose an approximate treatment of topography (ATT) for seafloor MT data for use in practical inversions of 3-D conductivity structures beneath the seafloor. It expresses conductivity using volumetric averaging in order to describe seafloor topography and uses improved interpolation methods to calculate MT responses at arbitrary points. Incorporating the ATT method into the WSINV3DMT program allowed the inversion code to be used with marine MT data. We conducted three types of synthetic tests and demonstrated that the ATT method behaves properly for marine MT datasets. We conclude that the ATT technique is suitable for use in 3-D inversions of seafloor MT data without causing large increases in the computational burden.

Acknowledgments. The authors would like to thank the editor (M. Hyodo), Katrin Schwalenberg, and an anonymous reviewer for useful comments. This research was partially supported by grants 16075204 from the Japanese Ministry of Education, Culture, Sports, Science and Technology (MEXT), and 220003 and 23740346 from the Japan Society of the Promotion of Science (JSPS). This research has been supported by the Thailand Research Fund (TRF:RMU5380018) to WS. Figures were produced using Generic Mapping Tools (GMT) software (Wessel and Smith, 1998). For this study, we used the computer systems of the Earthquake Information Center of the Earthquake Research Institute, the University of Tokyo.

Appendix A.

The eight magnetic field components denoted by gray arrows in Fig. 4 are calculated in the same way that magnetic fields are calculated in the WSINV3DMT (Siripunvaraporn

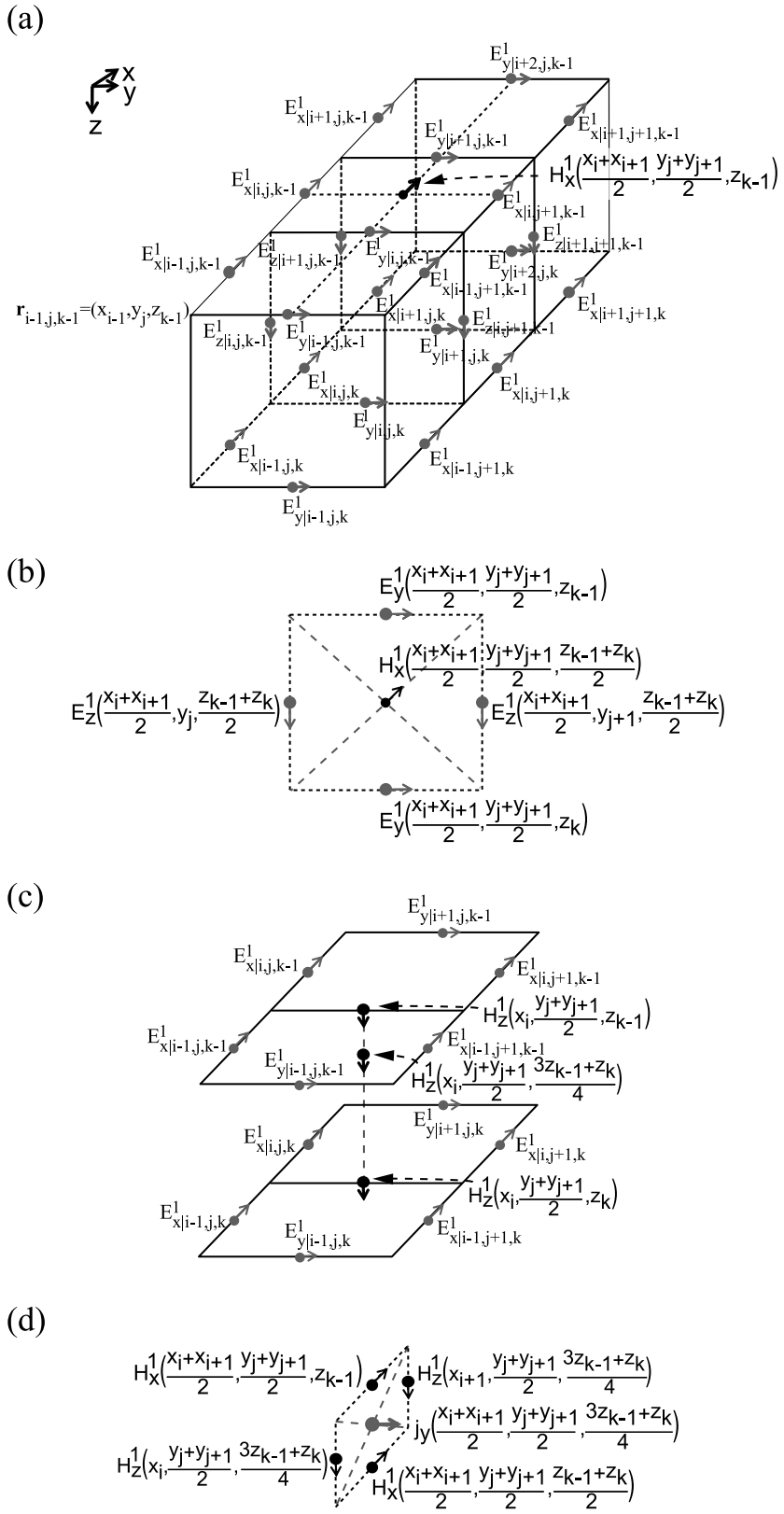

Fig. A.1. (a) Electric field components in the three-dimensional blocks used to calculate a magnetic field component in the WSINV3DMT. Gray arrows indicate electric field components on a three-dimensional staggered grid. A black arrow indicates an x-component of the magnetic field at the center of the block's top surface, which is used in the linear interpolation in (14) and (15). (b) Gray arrows located at the center of the edges indicate electric field components calculated from values on a three-dimensional staggered grid. A black arrow indicates an x-component of the magnetic field located in the center of a block. (c) Gray and black arrows indicate electric field components on a three-dimensional staggered grid and the z-components of the magnetic field, respectively. $H_z^1(x_i, \frac{y_j+y_{j+1}}{2}, z_{k-1})$ and $H_z^1(x_i, \frac{y_j+y_{j+1}}{2}, z_k)$ are located at the center of the edges. (d) Black and gray arrows indicate magnetic field components and a y-component of the electric current density, respectively.

et al., 2005). For instance, Fig. A.1(a) shows 24 electric field components (indicated by gray arrows) on a three-dimensional staggered grid. These are used to calculate $H_x^1(\frac{x_i+x_{i+1}}{2}, \frac{y_j+y_{j+1}}{2}, z_{k-1})$. First, $E_y^1(\frac{x_i+x_{i+1}}{2}, \frac{y_j+y_{j+1}}{2}, z_{k-1})$, denoted by a gray arrow in Fig. A.1(b), is calculated by interpolating $E^1_{y|i,j,k-1}$ and $E^1_{y|i+1,j,k-1}$. The other electric field components, denoted by gray arrows in Fig. A.1(b), are calculated the same way. Second, $H_x^1(\frac{x_i+x_{i+1}}{2}, \frac{y_j+y_{j+1}}{2}, \frac{z_{k-1}+z_k}{2})$, denoted by a black arrow in Fig. A.1(b), is calculated using Faraday's law from the four electric field components denoted by the gray arrows. Third, $H_z^1(x_i, \frac{y_j+y_{j+1}}{2}, z_{k-1})$ is calculated using Faraday's law with six electric field components, $E^1_{x|i-1,j,k-1}$, $E^1_{x|i-1,j+1,k-1}$, $E^1_{x|i,j,k-1}$, $E^1_{x|i,j+1,k-1}$, $E^1_{y|i-1,j,k-1}$, and $E^1_{y|i+1,j,k-1}$ in Fig. A.1(c). $H_z^1(x_i, \frac{y_j+y_{j+1}}{2}, z_k)$ is calculated in the same manner, and $H_z^1(x_i, \frac{y_j+y_{j+1}}{2}, z_{k-1})$ and $H_z^1(x_i, \frac{y_j+y_{j+1}}{2}, z_k)$ are interpolated to compute $H_z^1(x_i, \frac{y_j+y_{j+1}}{2}, \frac{3z_{k-1}+z_k}{4})$. $H_z^1(x_{i+1}, \frac{y_j+y_{j+1}}{2}, \frac{3z_{k-1}+z_k}{4})$ is calculated in the same way as $H_z^1(x_i, \frac{y_j+y_{j+1}}{2}, \frac{3z_{k-1}+z_k}{4})$. Fourth, $E_y^1(\frac{x_i+x_{i+1}}{2}, \frac{y_j+y_{j+1}}{2}, \frac{3z_{k-1}+z_k}{4})$ is calculated by interpolating $E^1_{y|i,j,k-1}$, $E^1_{y|i+1,j,k-1}$, $E^1_{y|i,j,k}$, and $E^1_{y|i+1,j,k}$. Then, a y-component of the electric current density, denoted by a gray arrow in Fig. A.1(d), $j_y(\frac{x_i+x_{i+1}}{2}, \frac{y_j+y_{j+1}}{2}, \frac{3z_{k-1}+z_k}{4})$, is converted from $E_y^1(\frac{x_i+x_{i+1}}{2}, \frac{y_j+y_{j+1}}{2}, \frac{3z_{k-1}+z_k}{4})$ using Ohm's law. Finally, $H_x^1(\frac{x_i+x_{i+1}}{2}, \frac{y_j+y_{j+1}}{2}, z_{k-1})$ is calculated using Ampere's law with three magnetic field components and one electric current density, as shown in Fig. A.1(d).

References

Baba, K. and A. D. Chave, Correction of seafloor magnetotelluric data for topographic effects during inversion, *J. Geophys. Res.*, **110**, B12105, doi:10.1029/2004JB003463, 2005.

Baba, K. and N. Seama, A new technique for the incorporation of seafloor topography in electromagnetic modelling, *Geophys. J. Int.*, **150**, 392–402, 2002.

Baba, K., A. D. Chave, R. L. Evans, G. Hirth, and R. L. Mackie, Mantle dynamics beneath the East Pacific Rise at 17°S: Insights from the Mantle Electromagnetic and Tomography (MELT) experiment, *J. Geophys. Res.*, **111**, B02101, doi:10.1029/2004JB003598, 2006.

Baba, K., H. Utada, T. Goto, T. Kasaya, H. Shimizu, and N. Tada, Electrical conductivity imaging of the Philippine Sea upper mantle using seafloor magnetotelluric data, *Phys. Earth Planet. Inter.*, **183**, 44–62, 2010.

Evans, R. L., P. Tarits, A. D. Chave, A. White, G. Heinson, J. H. Filloux, H. Toh, N. Seama, H. Utada, J. R. Booker, and M. J. Unsworth, Asymmetric electrical structure in the mantle beneath the East Pacific Rise at 17°S, *Science*, **286**, 752–756, 1999.

Filloux, J. H., Techniques and instrumentations for study of natural electromagnetic induction at sea, *Phys. Earth Planet. Inter.*, **7**, 323–338, 1973.

Filloux, J. H., Magnetotelluric exploration of the North Pacific: Progress report and preliminary soundings near a spreading ridge, *Phys. Earth Planet. Inter.*, **25**, 187–195, 1981.

Li, S., J. R. Booker, and C. Aprea, Inversion of magnetotelluric data in the presence of strong bathymetry/topography, *Geophys. Prospect.*, **56**, 259–268, 2008.

Matsuno, T., N. Seama, R. L. Evans, A. D. Chave, K. Baba, A. White, T. Goto, G. Heinson, G. Boren, A. Yoneda, and H. Utada, Upper mantle electrical resistivity structure beneath the central Mariana subduction system, *Geochem. Geophys. Geosyst.*, **11**, Q090003, doi:10.1029/2010GC003101, 2010.

Nam, M. J., H. J. Kim, Y. Song, T. J. Lee, and J. H. Suh, Three-dimensional topography corrections of magnetotelluric data, *Geophys. J. Int.*, **174**, 464–474, 2008.

Newman, G. A. and D. L. Alumbaugh, Three-dimensional magnetotelluric inversion using non-linear conjugate gradients, *Geophys. J. Int.*, **140**, 410–424, 2000.

Nolasco, R., P. Tarts, J. H. Filloux, and A. D. Chave, Magnetotelluric imaging of the Society Islands hotspot, *J. Geophys. Res.*, **103**, 30,287–30,309, 1998.

Oldenburg, D. W., Conductivity structure of oceanic upper mantle beneath the Pacific plate, *Geophys. J. R. Astron. Soc.*, **65**, 359–394, 1981.

Schwalenberg, K. and R. N. Edwards, The effect of seafloor topography on magnetotelluric fields: An analytical formulation confirmed with numerical results, *Geophys. J. Int.*, **159**, 607–621, 2004.

Siripunvaraporn, W., G. Egbert, Y. Lenbury, and M. Uyeshima, Three-dimensional magnetotelluric inversion: Data-space method, *Phys. Earth Planet. Inter.*, **150**, 3–14, 2005.

Smith, W. H. and D. T. Sandwell, Bathymetric prediction from dense altimetry and sparse shipboard bathymetry, *J. Geophys. Res.*, **99**, 21,803–21,824, 1994.

Wessel, P. and W. H. F. Smith, New, improved version of the generic mapping tools released, *Eos Trans. AGU*, **79**, 579, 1998.

Yoshino, T., Laboratory electrical conductivity measurement of mantle minerals, *Surv. Geophys.*, **31**, 163–206, 2010.

Yoshino, T., M. Laumonier, E. Mclsaac, and T. Katsura, Electrical conductivity of basaltic and carbonatite melt-bearing peridotites at high pressures: Implications for melt distribution and melt fraction in the upper mantle, *Earth Planet. Sci. Lett.*, **295**, 593–602, 2010.

Zhang, L., T. Koyama, H. Utada, P. Yu, and J. Wang, A regularized three-dimensional magnetotelluric inversion with minimum gradient support constraint, *Geophys. J. Int.*, 1–21, doi:10.1111/j.1365-246X.2012.05379.x, 2012.

N. Tada (e-mail: norikot@jamstec.go.jp), K. Baba, W. Siripunvaraporn, M. Uyeshima, and H. Utada